buildings

MDPI

Article

The Effect of Fly Ash on the Microstructural Evolution and Mechanical Properties of Geopolymers Made from Phosphorus Tailings and Ground Granulated Blast-Furnace Slag

Yunrui Zhao [1], Zhou Wang [1], Jie Wu [1], Qiancheng Ding [1], Hui Luo [1,*] and Bao-Jie He [2,3,*]

[1] School of Civil and Ocean Engineering, Jiangsu Ocean University, Lianyungang 222005, China; zhaoyr997997@163.com (Y.Z.); 19850959378@163.com (Z.W.); 18952043929@163.com (J.W.); ding_031@163.com (Q.D.)
[2] Centre for Climate-Resilient and Low-Carbon Cities, Key Laboratory of New Technology for Construction of Cities in Mountain Area, School of Architecture and Urban Planning, Ministry of Education, Chongqing University, Chongqing 400045, China
[3] School of Architecture, Design and Planning, University of Queensland, Brisbane, QLD 4067, Australia
* Correspondence: water@njfu.edu.cn (H.L.); baojie.he@cqu.edu.cn (B.-J.H.)

Abstract

Severe environmental contamination from accumulated phosphorus tailings and their low recycling rate remain critical bottlenecks in solid waste treatment. Furthermore, geopolymers fabricated using single or binary solid wastes generally suffer from insufficient mechanical properties and poor durability, while their synergistic activation mechanisms have not been fully clarified. To address these issues, this study developed a binary geopolymers composite using phosphorus tailings and ground granulated blast furnace slag (GGBS) as raw materials through alkali activation (sodium hydroxide and water-glass), and prepared a ternary geopolymers composite incorporating fly ash. The effects of solid waste blending ratios on flowability, compressive strength, drying–wetting and freeze–thaw resistance as well as drying shrinkage were systematically investigated, and the synergistic geopolymerization mechanism was characterized by SEM-EDS, XRD and FTIR. Experimental results show that the binary system achieves optimal performance at 40% GGBS substitution, yielding a 28-day compressive strength of 23.4 MPa with lower shrinkage and better anti-damage capacity than pure phosphorus tailings specimens. Introducing 20% fly ash into the optimized binary system forms a ternary geopolymer with a 28-day strength of 37.8 MPa, rising by 61.5%. Its drying shrinkage, mass loss from drying–wetting cycles and freeze–thaw erosion are separately reduced by 33.3%, 39.5% and 40.0%. Microscopic analyses verify that GGBS and fly ash collaboratively provide active Ca, Si and Al species to stimulate abundant C-S-H gel formation and compact the matrix microstructure. This ternary geopolymer realizes efficient collaborative utilization of three industrial solid wastes, providing theoretical support and technical guidance for large-scale resource utilization of phosphorus tailings and the fabrication of geopolymer construction materials.

Keywords: phosphorus tailings; ground granulated blast-furnace slag; fly ash; binary geopolymers; ternary geopolymers

Check for updates

Academic Editors: Ayman El-Zohairy and Ahmed A. Ibrahim

Received: 6 August 2026
Revised: 12 September 2026
Accepted: 15 September 2026
Published: 16 September 2026

Copyright: © 2026 by the authors. Licensee MDPI, Basel, Switzerland. This article is an open access article distributed under the terms and conditions of the Creative Commons Attribution (CC BY) license.

1. Introduction

As China accelerates infrastructure development and fully promotes the implementation of the Dual Carbon goals, traditional Portland cement construction materials are exposing increasingly obvious inherent deficiencies, including high energy consumption,

substantial carbon emissions and excessive consumption of natural resources. Accordingly, the development of low-carbon, eco-friendly and high-performance novel cementitious materials has evolved into a core research hotspot within the field of construction materials [1]. As a vital strategic mineral resource in China, phosphorus ore is extensively utilized in phosphorus fertilizer production, fine phosphorus chemical industry and other sectors. Substantial phosphorus tailings are discharged during the flotation and processing of phosphorus ores. Relevant statistical data show that the annual output of phosphorus tailings in China exceeds ten million tons, and the total accumulated stock has reached hundreds of millions of tons, while the comprehensive utilization efficiency of such solid waste is still lower than 10 percent [2]. Mass-scale phosphorus tailings (PT) deposited in open-air piles over extended periods take up vast land areas. Meanwhile, phosphorus, fluorine and trace heavy metal constituents within these tailings can leach out under rainfall infiltration, which further gives rise to ecological risks such as soil pollution and water environment deterioration [3]. Furthermore, valuable mineral constituents such as silicon, calcium and magnesium abundant in phosphorus tailings are left unutilized, leading to severe resource waste. Hence, it is urgent to develop efficient and large-scale approaches for their resource reclamation [4]. Meanwhile, ground granulated blast-furnace slag (GGBS) and fly ash (FA) are massive industrial solid wastes discharged from the iron and steel and thermal power industries, with annual output reaching hundreds of millions of tons [5]. Conventional disposal methods including landfill and low-value blending application deliver low economic added value and limited utilization efficiency. Realizing synergistic resource utilization of multiple industrial solid wastes therefore constitutes a critical issue to be urgently addressed in solid waste treatment and green building material industries.

Considerable progress has been achieved in domestic and overseas research regarding geopolymers fabricated with single component or binary blends of phosphorus tailings, GGBS and fly ash at the present stage. Most existing studies have focused on the optimization of mix proportions and the modulation of macroscopic mechanical properties in alkali-activated systems based on a single type of solid waste, as well as on the analysis of performance matching for binary solid waste combinations. Obeng et al. increased the maximum compressive strength from 20.06 MPa to 25.3 MPa by adding calcium carbide residue to a kaolin-based polymer, representing an increase of 20.7% [6]. Moukannaa et al. replaced fly ash with phosphorus sludge, which reduced the performance of the samples but still resulted in a relatively high strength (62 MPa). This suggests that the use of phosphorus tailings in geopolymers could serve as a viable technical solution [3]. Zheng et al. found that when phosphorus tailings were added to Polish cement, a small proportion of the phosphorus dissolved during the reaction; however, this did not result in significant volume expansion or a reduction in strength [7]. These studies fully validate the application potential of soil–polymer composites made from solid waste as alternatives to traditional cementitious materials. Nevertheless, obvious deficiencies and limitations still exist in current studies. Firstly, pure phosphorus tailings exhibit low reactivity and unbalanced silicon–aluminum compositions; geopolymers prepared solely from phosphorus tailings suffer from slow strength development, poor workability and unsatisfactory durability [4]. Secondly, binary solid waste blended systems possess limited component complementarity. For instance, fly ash is rich in silicon and aluminum phases yet contributes little to early-age strength gain [8]. In contrast, mineral powder contains abundant calcium-bearing phases, which can accelerate the geopolymerization reaction and boost early mechanical strength [9]. Accordingly, constructing ternary composite systems by incorporating different types of solid wastes enables structural optimization of the matrix by virtue of the respective advantages of each raw material [10].

As an innovative low-carbon technology for the resource utilization of solid wastes, alkali-activated geopolymerization technology boasts prominent merits including mild reaction conditions, high solid waste consumption rate, low carbon emission, as well as dense and stable microstructure of hardened products. It has emerged as a pivotal technique to substitute conventional cementitious systems and realize high-value utilization of industrial solid wastes [11]. Compared with traditional treatment methods such as high-temperature sintering and simple blending modification, alkaline activation is capable of activating inert silicon–aluminum mineral phases inside solid wastes under alkaline surroundings. It drives the depolymerization-condensation reactions of active species to form a three-dimensional network inorganic gel framework, thereby remarkably improving the mechanical performance, compactness and corrosion resistance of solid waste-derived materials [12]. This technology effectively addresses the insufficient reactivity of natural minerals and the unsatisfactory performance arising from the separate utilization of single-type solid waste. This offers a technically viable scientific pathway for fabricating high-performance geopolymers via combined utilization of multiple types of industrial solid wastes. Accordingly, it has gained widespread research interest and undergone fast-growing progress within solid-waste recovery and eco-friendly construction material domains over recent years.

In view of the deficiencies of existing research, this work takes massively stockpiled and difficult-to-recycle phosphorus tailings as the primary raw material, combines high-reactivity mineral powder and fly ash to form a ternary solid waste system, and adopts the alkali-activated geopolymerization process to fabricate novel composite geopolymer materials. The influences of raw material mixing ratios on the macroscopic mechanical properties and durability of the prepared materials are systematically investigated. Combined with microscopic characterization techniques including SEM-EDS, XRD and FTIR, this study elaborates the geopolymerization reaction mechanism under synergistic alkali activation of binary and ternary solid wastes, the evolution characteristics of gel products as well as the formation mechanism of microstructures, and clarifies the internal correlation between macroscopic performances and microscopic structures. This study innovatively constructs a ternary alkali-activated geopolymer system consisting of phosphorus tailings, mineral powder and fly ash. It achieves high-value co-utilization for diverse industrial solid wastes, which is capable of supplying theoretical foundations and technical references for resource recycling of bulk solid residues represented by phosphorus tailings, as well as the future development of potential geopolymer-based construction materials derived from solid wastes.

2. Materials and Methods

2.1. Solid Waste Materials and Chemical Reagents

Phosphorus tailings (PT) are solid wastes generated during phosphorus ore beneficiation, which rank among the largest-volume solid wastes discharged by the phosphorus chemical industry. The phosphorus tailings adopted in this work were collected from the tailings pond of Jinping Phosphorus Mine in Lianyungang, Jiangsu Province, China. Raw phosphorus tailing samples were thermally treated inside an electric drying oven at 105 °C over a 24 h period. Afterward, the materials underwent 40 min of grinding using a planetary ball mill, followed by screening with a 0.075 mm standard sieve to obtain reserved test materials, as illustrated in Figure 1a. Ground granulated blast-furnace slag (GGBS) refers to fine particulate industrial solid waste produced in metallurgical manufacturing, mainly composed of silicon oxides along with trace heavy metal elements. S95-grade GGBS supplied by Hanjiang Mining Technology Co., Ltd., Lianyungang, China, was used in this experiment, as shown in Figure 1b. Fly ash (FA) is fine powdered solid waste captured from flue gas after pulverized coal combustion in coal-fired power plants and other coal-burning

enterprises. It is one of the industrial solid wastes with the highest annual output and most mature comprehensive utilization technologies in China. The fly ash used herein was obtained from Lianyungang Xinneng Sludge Power Generation Co., Ltd., Lianyungang, China, as illustrated in Figure 1c. Sodium hydroxide pellets with a purity of 96% manufactured by Xilong Scientific Co., Ltd., Shanghai, China, were employed as the alkaline activator. The sodium silicate solution adopted in this study was supplied by Linsen Chemical Co., Ltd., (Linyi, China), possessing an original silicate modulus of 1.45. X-ray fluorescence (XRF) measurement was performed to characterize the major chemical constituents of each raw material, and the acquired testing outcomes are compiled in Table 1.

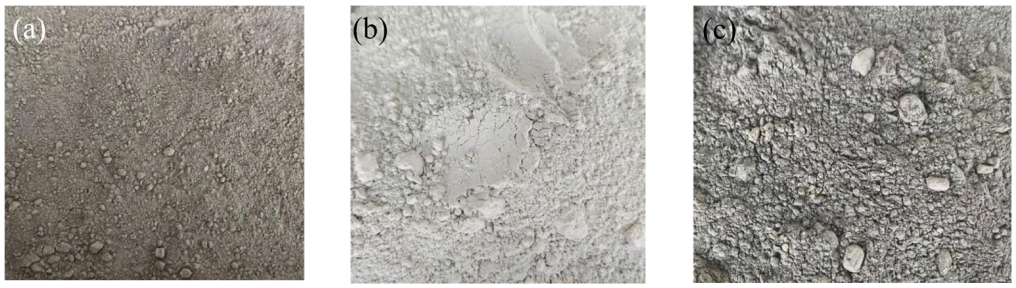


Figure 1. Solid waste materials: (**a**) PT, (**b**) GGBS, (**c**) FA.

Table 1. Substance composition in PT, GGBS and FA.

Materials	CaO	SiO_2	Al_2O_3	Fe_2O_3	SO_3	MgO	TiO_2	P_2O_5	Na_2O	LOI
PT	2.9	53.1	24.9	1.95	1.25	3.1	1.55	1.48	0.45	7.6
GGBS	36.6	31.1	16.8	0.35	2.3	9	1	-	0.85	0.43
FA	4.6	46.9	33.9	3.4	1.1	0.65	1.6	0.42	2.3	1.55

The results of the mineral phase analysis are shown in Figure 2. Quartz is the predominant crystalline phase in the phosphorus tailings, whilst the crystalline minerals dolomite and fluorapatite can also be detected. Dolomite and fluorapatite exhibit sharp diffraction peaks, indicating that the grains of these minerals are well crystallized. Residual phosphorus in phosphorus tailings primarily exists in the form of fluorapatite. The phase composition of GGBS is predominantly quartz, whilst calcium (Ca) is present in the form of calcium oxide within the glass phase, appearing as a broad, diffuse peak spanning 25–35°. Fly ash consists of quartz, mullite and calcite with relatively weak diffraction peaks; the glassy phase generated during high-temperature calcination serves as the essential source of its pozzolanic activity. The particle size distribution curves presented in Figure 2d–f demonstrate that the particle sizes of the three raw materials exhibit complementary gradation effects. Figure 2g–i illustrate the micromorphology of raw materials. Phosphorus tailings exist as irregular massive aggregates with rough and porous surfaces interspersed with acicular fluorapatite crystals. Such structural features endow phosphorus tailings with a large specific surface area and sufficient reaction interfaces; nevertheless, their high crystallinity leads to inherently low geopolymerization activity. GGBS consists of angular homogeneous particles with dense surfaces, whose reactivity can only be activated via erosion by alkaline solutions. The abundant calcium-containing components in GGBS facilitate the formation of hydrated cementitious products. Fly ash is mainly composed of spherical glass microspheres mixed with flocculent agglomerates. These spherical particles are beneficial to improving the workability of fresh paste and reducing water demand. The reactive silicon and aluminum components present in the glassy phase, together with

the large specific surface area of aggregate particles, create favorable conditions for the progression of alkali-activation reactions.

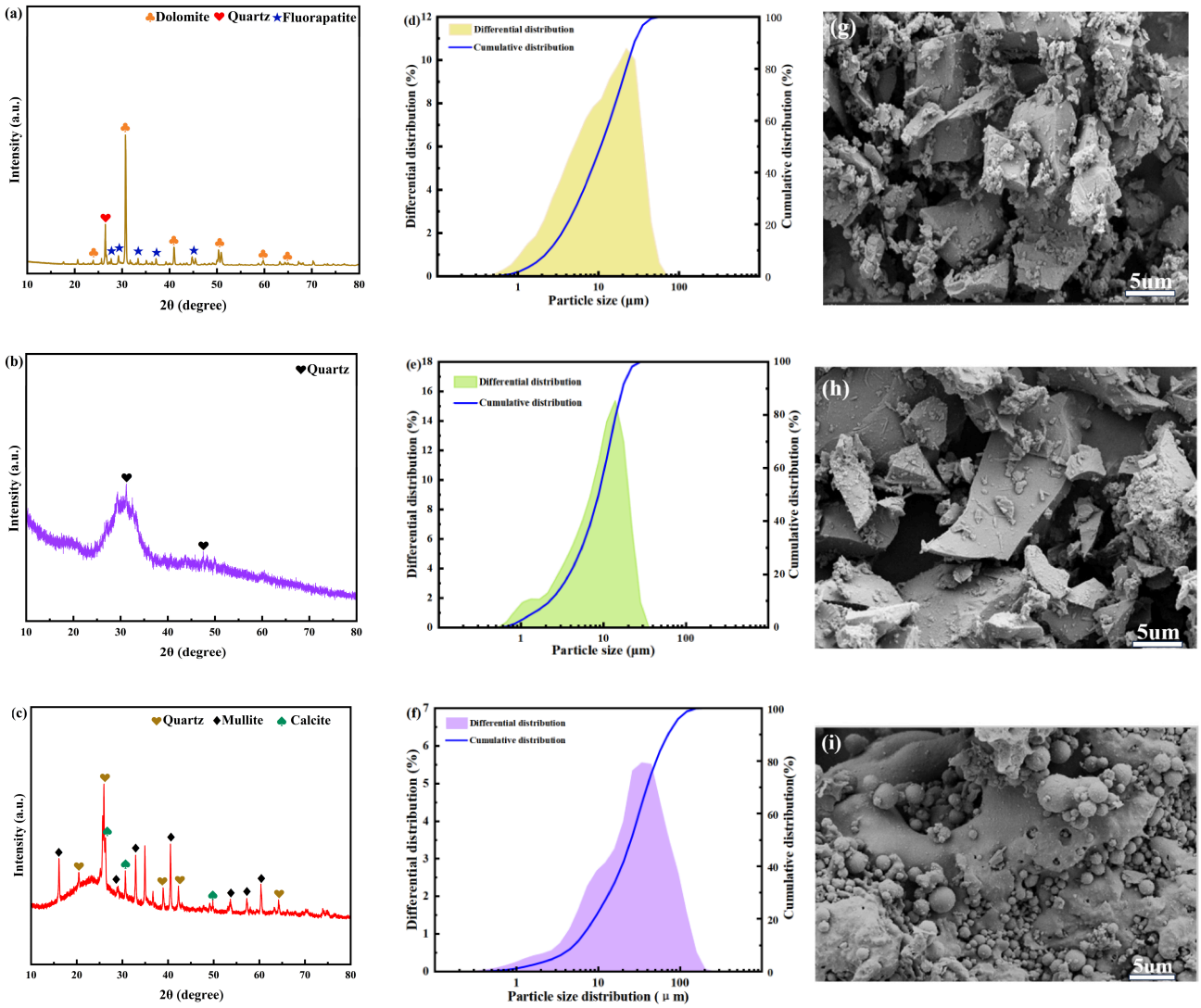


Figure 2. XRD of PT (**a**), GGBS (**b**), FA (**c**). Particle size distribution of PT (**d**), GGBS (**e**), FA (**f**). SEM of raw materials of PT (**g**), GGBS (**h**), FA (**i**).

2.2. Preparation Method

The preparation procedure of PT-based geopolymer cementitious materials in this study was implemented in accordance with the requirements specified in GB/T 17671—2021 Method of testing cements, Determination of strength (ISO method) [13]. Firstly, 20 g of analytically pure sodium hydroxide pellets were weighed and transferred into a dry beaker. A certain amount of deionized water was added according to the preset water-to-binder ratio, followed by stirring until complete dissolution. The mixture was kept static for 2 h to prepare the alkaline NaOH activator solution. Subsequently, PT, GGBS and FA that had been dried and sieved were weighed in accordance with the mixing proportions listed in Table 2. The three powder raw materials were firstly dry-mixed in a mortar mixer for 60 s to achieve sufficient dispersion and homogeneous mixing. Afterwards, the prepared sodium hydroxide solution was added and mixed continuously for 120 s, followed by the addition of quantified water glass solution (mass fraction of Na_2O: 12.8 wt%, mass fraction of SiO_2: 18.6 wt%, water content: 68.6 wt%) with another 120 s of stirring to guarantee thorough homogenization of the fresh paste without agglomeration. Upon the completion of stirring,

the fresh mixture was poured into standard three-gang prismatic molds with dimensions of 40 × 40 × 160 mm, whose inner surfaces were pre-coated with release agent. The filled molds were vibrated on a vibration table for 60 s to expel entrapped air bubbles inside the paste. After vibration, the specimens were placed indoors under shade for static curing, and demolding was conducted after 12 h. The demolded samples were transferred into a standard curing chamber, where the curing temperature was maintained at (20 ± 2) °C and the relative humidity was controlled above 98%. Specimens were cured for target ages of 1 day, 7 days and 28 days separately. In the binary system, PG1 was used as the control group; in the ternary system, PG5 was used as the control group.

Table 2. Mixing ratio design for cementitious materials.

System	Sample	Phosphorus Tailings Content (%)	GGBS Content (%)	FA Content (%)	Water Glass Content (%)	Water-to-Binder Ratio
Phosphorus tailings–ore powder binary system	PG1	100	-	-	24	0.35
	PG2	90	10			
	PG3	80	20			
	PG4	70	30			
	PG5	60	40			
	PG6	50	50			
Phosphorus tailings–ore powder–FA ternary system	PGF1	60	36	4		
	PGF2	60	32	8		
	PGF3	60	28	12		
	PGF4	60	24	16		
	PGF5	60	20	20		
	PGF6	60	16	24		

Note: Binder = total solid-waste powder mass (PT + GGBS + FA). Total mixing water includes de-ionized water for dissolving NaOH plus the inherent water fraction introduced by commercial sodium-silicate solution. Water-glass dosage of 24% refers to mass percentage relative to total solid binder mass. The dose of alkali activator is a fixed value.

2.3. Test Methods

The fluidity test was carried out in accordance with the requirements specified in Methods for testing uniformity of concrete admixtures (GB/T 8077-2023) [14]. A frustoconical mold with dimensions of Φ36 mm × 60 mm × 60 mm was adopted to test the fluidity of the prepared cementitious materials. The thoroughly mixed fresh cement slurry was poured into the flow test mold and the surface was leveled. Afterwards, the mold was lifted vertically by 5–10 cm within 2 s, and the paste was allowed to flow freely for 30 s under static condition. After the flow shape became stable, the maximum spreading diameters along two mutually perpendicular directions were measured with a vernier caliper. Each group was tested using three parallel specimens, and the arithmetic mean was calculated. The measurement accuracy was 0.1 mm.

A SANS universal testing machine was employed in this experiment, featuring a displacement accuracy of ±0.01 mm and a force measurement accuracy within ±0.5%. The compressive strength tests of geopolymer specimens were implemented referring to Method of testing cements, Determination of strength (ISO method) (GB/T 17671-2021) [13]. Test specimens measuring 40 mm × 40 mm × 160 mm were used in the compressive strength

test. Each group comprised three parallel specimens, and the optimum mix proportion was determined based on the strength results. The calculation formula is as follows:

$$P = \frac{F}{A} \tag{1}$$

where P denotes the compressive strength (MPa), F is the maximum failure load applied on the specimen (N), and A represents the contact area between the specimen and the bearing plate (mm^2).

The drying shrinkage test was conducted in accordance with Standard for test method of basic properties of construction mortar (JGJ/T 70-2009) [15]. After 24 h of standard curing, the initial length and initial mass of specimens were measured. Thereafter, the specimens were subjected to drying treatment under constant temperature and constant humidity environments, and their lengths were tested at different curing ages. Each group comprised three parallel specimens. The drying shrinkage rate and mass loss rate of the cementitious material at age T were calculated using Equation (2) and Equation (3), respectively.

$$S_t = \frac{L_0 - L_t}{L} \times 100\% \tag{2}$$

$$M_l = \frac{M_0 - M_t}{M_0} \times 100\% \tag{3}$$

where S_t is the drying shrinkage rate (%), L_0 stands for the initial length (mm), L_t refers to the specimen length at age T (mm), and L is the effective gauge length of the specimen fixed at 160 mm. M_l denotes the mass loss rate (%), M_0 is the initial mass (g), and Mt is the specimen mass measured at age T (g).

The drying–wetting cycle test was implemented in accordance with Standard for test methods of long-term performance and durability of ordinary concrete (GB/T 50082-2009) [16]. During the test procedure, specimens were first immersed in a constant-temperature water tank for soaking treatment. Subsequently, the saturated specimens were transferred into an electric blast drying oven for drying, followed by natural cooling in a shaded indoor environment after being taken out. Upon the completion of each cycle, specimens were cooled down to room temperature. Their surface morphology was visually inspected, the mass of each specimen was weighed, and the corresponding mass loss rate was calculated accordingly. Three parallel specimens were tested in each series of experiments.

$$\Delta M_a = \frac{m_t - m_n}{m_t} \times 100\% \tag{4}$$

where ΔM_a represents the mass loss rate of specimens after N drying–wetting cycles (%), m_t is the mass of specimens prior to the drying–wetting test (g), and m_n denotes the specimen mass after N drying–wetting cycles (g).

The freeze–thaw cycle test was carried out in accordance with Standard for test methods of long-term performance and durability of ordinary concrete (GB/T 50082-2009) [16]. Specimens were immersed in water for 2 h to reach a water-saturated state in advance, and then placed into an accelerated concrete freeze–thaw testing machine for the freeze–thaw cycle test. After the completion of each single cycle, the specimens were taken out, surface moisture was wiped off thoroughly, their mass was weighed, and the mass loss rate was calculated subsequently. Each set of experiments comprised three parallel specimens.

$$\Delta W_a = \frac{W_0 - W_n}{W_0} \times 100\% \tag{5}$$

where W_a is the mass loss rate of specimens after N freeze–thaw cycles (%), W_0 refers to the mass of specimens before the freeze–thaw test (g), and W_n stands for the mass of specimens after N freeze–thaw cycles (g).

2.4. Microscopic Testing Methods

A CMT5504 universal testing machine was utilized to characterize the macroscopic mechanical properties of geopolymers, so as to establish the correlation between macroscopic performances and microscopic structures. A Gemini SEM 300 scanning electron microscope (SEM) was adopted to observe the micromorphology, pore structure and interfacial bonding characteristics of geopolymer matrices. A D8 Advance X-ray diffractometer (XRD) was employed to analyze crystalline and amorphous phase assemblages and reveal the evolution law of mineral phases during geopolymerization. A Thermo Scientific Nicolet iS50 Fourier transform infrared spectrometer (FTIR) was used to interpret the molecular mechanism of geopolymerization reactions via the identification of functional groups and chemical bonds.

3. Results and Discussion

3.1. Properties of Binary Geopolymers

3.1.1. The Flowability and Compressive Strength of PG

Figure 3a illustrates the fluidity performance of binary geopolymer binder systems. Test results indicate that increasing the GGBS incorporation amount leads to a gradual reduction in the fluidity of these composite mixtures. The pure PT group (PG1) achieves the maximum fluidity of 238 mm. As the replacement ratio of GGBS rises sequentially from 10% to 50%, the fluidity declines continuously to 226 mm, 209 mm, 195 mm and 186 mm, and finally reaches 178 mm at a GGBS dosage of 50%, with an overall reduction of 25.2%. This phenomenon can be tentatively explained from two aspects. On the one hand, GGBS possesses a much larger specific surface area than PT, which adsorbs a larger amount of free water and reduces the free water available for lubricating solid particles. The variation in water film thickness is closely associated with the adsorption capacity of particle surfaces towards free water [17]. On the other hand, PT contain abundant inert components such as dolomite and fluorapatite. A higher proportion of PT corresponds to lower contents of reactive SiO_2 and Al_2O_3 in the system, leading to a slower hydration reaction rate [4]. Accordingly, the dosage of GGBS exhibits a negative correlation with the fluidity of the binary PT-GGBS cementitious system.

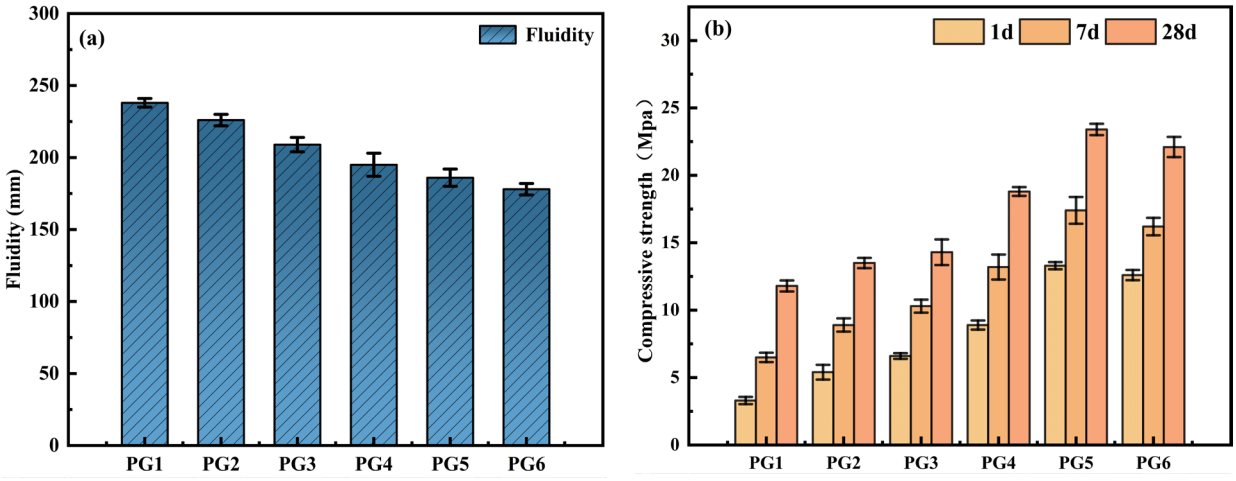


Figure 3. (**a**) Flowability and (**b**) compressive strength of a binary cementitious material composed of phosphorus tailings and GGBS.

Figure 3b illustrates the compressive strength of the binary PT-GGBS specimens cured for different ages. The pure PT sample (PG1) shows the lowest compressive strength values at 1 day, 7 days and 28 days, which are merely 3.3 MPa, 6.5 MPa and 11.8 MPa, respectively.

This result verifies that PT have intrinsically low hydration reactivity and poor cementing performance. The incorporation of GGBS contributes to a significant initial improvement in compressive strength, followed by a mild decline. The specimen with 40% GGBS content (PG5) achieves the optimal mechanical performance, with compressive strengths reaching 13.3 MPa, 17.4 MPa and 23.4 MPa after 1, 7 and 28 days of curing, respectively. These values are elevated by 303.0%, 167.7% and 98.3% compared with the pure PT group, showing a considerable strengthening effect compared with the PG1. It indicates that GGBS possesses considerable latent hydration activity and can effectively participate in geopolymerization under alkaline activation. Meanwhile, it optimizes the particle gradation of the matrix and improves matrix compactness, thereby enhancing the overall mechanical performance of composites. Nevertheless, when the dosage of GGBS exceeds 40%, the compressive strengths decline to 12.6 MPa, 16.2 MPa and 22.1 MPa at 1 day, 7 days and 28 days, representing reductions of 5.3%, 6.9% and 5.6% relative to the optimal mixture. It is hypothesized that two factors account for this strength drop. First, with fixed-dosage alkaline activators, increasing GGBS content may result in relative limitation of available alkalis for activating surplus GGBS. Under this circumstance, part of GGBS might merely serve as an inert physical filler instead of fully engaging in hydration reactions [18]. Second, an overly-high dosage may disturb the optimal particle gradation between PT and GGBS, which presumably slightly increases internal porosity and results in a mild drop in mechanical strength [19]. This hypothesis is partially supported by subsequent micro-characterization results. For PG1 and PG5 in the binary system, the standard deviation and coefficient of variation for the 28-day compressive strength values were (SD = 0.41 MPa, CV = 3.47%) and (SD = 0.42 MPa, CV = 1.79%), respectively. The coefficients of variation generally fell within an acceptable range, indicating satisfactory repeatability of the compressive strength.

3.1.2. The Drying Shrinkage and Mass Loss of PG

Figure 4 depicts the changes in drying shrinkage and mass loss of binary geopolymer, which reflects the effects of GGBS dosage on the volume stability and anti-shrinkage performance of geopolymer matrices during the drying process. Drying shrinkage describes the dimensional deformation of a specimen caused by capillary tension and microstructural rearrangement during the evaporation of moisture. Mass loss quantifies the reduction in the specimen's mass, primarily reflecting the evaporation of moisture and the flaking of surface material during cyclic testing. As shown in Figure 4a, the specimen consisting of 100% PT (PG1) exhibits the most drastic growth in shrinkage, with a 30-day drying shrinkage rate reaching 1.94%, the maximum value among all binary mixtures. The drying shrinkage rate shows a marked decrease with increasing GGBS dosage. At a GGBS dosage of 40% (PG5), the 30-day shrinkage rate is only 1.14%, which is reduced by 41.2% compared with the pure PT group. In addition, the proportion of shrinkage developed within the first 10 days drops to 36%. This phenomenon can be tentatively explained by the formation of C-S-H gels during the hydration of GGBS; these gel phases presumably refine the pore structure, restrain internal deformation and slow down the evaporation of free water, thereby mitigating drying shrinkage. Nevertheless, when the GGBS dosage exceeds 40%, the 30-day drying shrinkage rate rebounds to 1.69%. It is hypothesized that the relatively limited supply of alkalis (at fixed activator dosage) may fail to fully activate excessive GGBS, which in turn contributes to the rebound of drying shrinkage.

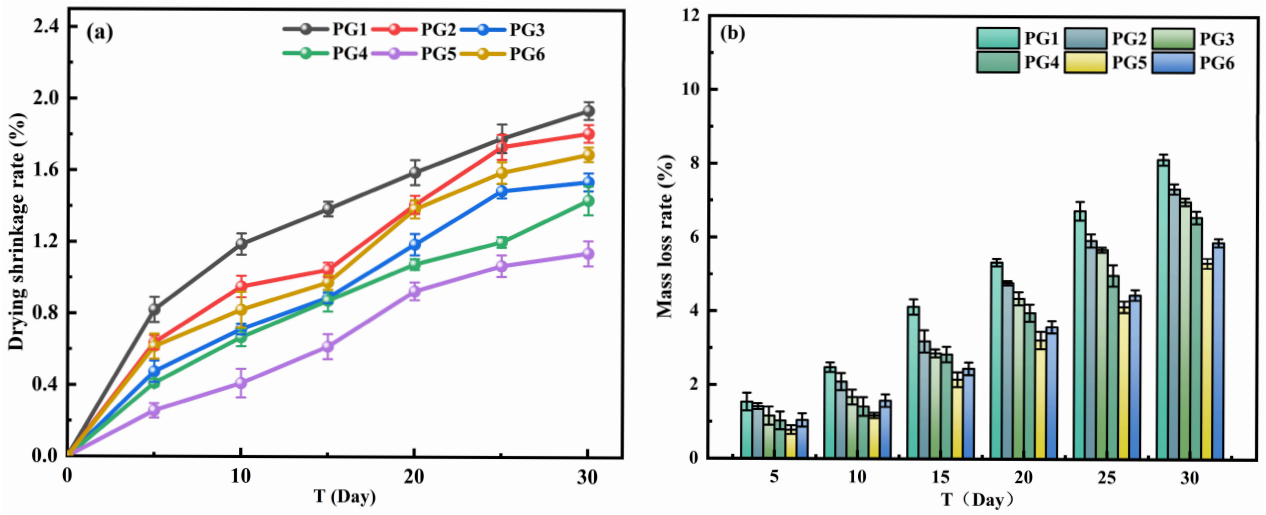


Figure 4. Drying shrinkage and mass loss characteristics of PT-GGBS binary binder systems: (**a**) Drying shrinkage behavior of binary geopolymer binders; (**b**) Mass loss ratio of binary geopolymer binders.

It can be seen from Figure 4b that the pure PT group (PG1) also possesses the highest mass loss rate in the whole system, with a cumulative 30-day mass loss of 8.13%, 30.45% of which occurs within the initial 10 days. Severe early-stage water evaporation and surface spalling are observed in this sample. The mass loss rate declines obviously with the rising dosage of GGBS; the 30-day mass loss of sample PG5 decreases to 5.32%, representing a reduction of 34.6% relative to PG1. This verifies that appropriate dosage of GGBS generates hydration gels to fill internal pores and improve the structural stability against drying shrinkage. However, once the GGBS content exceeds 40%, the 30-day mass loss increases to 5.88%, which is 10.5% higher than that of PG5. In summary, moderate incorporation of GGBS presumably produces gel products to block water-evaporation pathways, strengthen inter-particle bonding and lower the possibility of surface spalling. By contrast, excessive GGBS may disrupt the optimal particle gradation and deteriorate matrix compactness, accelerating water evaporation and increasing surface-peeling risk [20].

3.1.3. The Mass Loss During the Wet–Dry Cycle of PG

Figure 5 shows the mass loss rate of PT-GGBS binary cementitious materials subjected to drying–wetting cycles. It can be observed that the mass loss rate of all specimens rises gradually with the increase in the number of drying–wetting cycles, and obvious discrepancies exist among different mixing proportions. Within 0–10 cycles, the mass loss of all samples increases moderately, with the increment lower than 2.5 percentage points. After 10 cycles, the mass loss rate of PG1 reaches 3.4%, while that of PG5 is only 1.3%. The growth rate of mass loss accelerates remarkably from 10 to 25 cycles, which constitutes the dominant stage of mass deterioration. The mass loss rate of PG1 climbs from 3.4% to 11.0%, with an increment of 7.6 percentage points accounting for 64.4% of the total mass loss after 30 cycles; the increments of PG2–PG6 also exceed five percentage points. During 25–30 cycles, the rising rate of mass loss slows and the degradation tendency tends to stabilize. The mass loss rate of PG1 merely increases from 11.0% to 11.8% (an increment of 0.8 percentage points), and the increments of the remaining groups are all less than two percentage points.

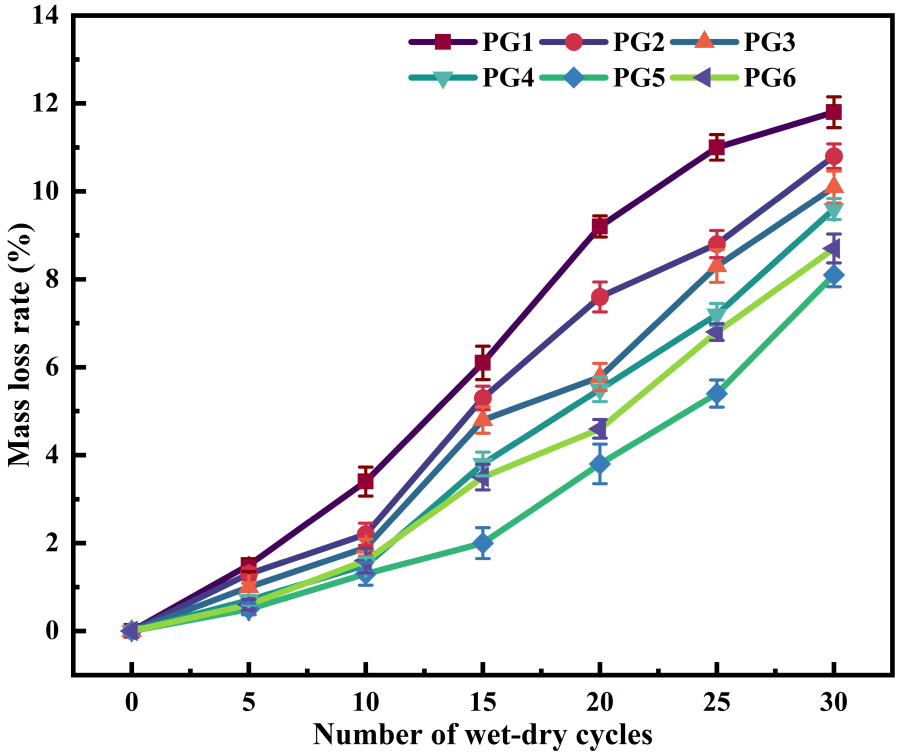


Figure 5. Mass loss rate of PT-GGBS binary cementitious material during wet–dry cycle.

Overall, the mass loss rate is closely correlated with the dosage of GGBS; higher GGBS dosage corresponds to lower mass loss of specimens. Specifically, PG1 exhibits the highest mass loss at all stages, reaching 11.8% after 30 cycles. PG5 maintains the lowest mass loss throughout the whole test process, which is only 8.1% after 30 cycles, 31.4% lower than PG1, and its mass loss rate at each stage is inferior to other groups. The mass loss rates of PG2–PG4 and PG6 fall between those of PG1 and PG5 and decrease stepwise with the rising dosage of GGBS. This phenomenon can be tentatively attributed to the pozzolanic-activity effect and particle-filling effect brought by GGBS [21,22]. Accordingly, the incorporation of GGBS effectively improves the resistance of binary PT-GGBS cementitious materials against drying–wetting cyclic deterioration.

3.1.4. The Resistance to Freeze–Thaw Cycles of PG

This study analyzes the mass loss changes of PT-GGBS binary binder composites under freeze–thaw cycling conditions, as demonstrated in Figure 6. The results show that the mass loss ratio of the binary binder system rises continuously as the freeze–thaw cycle number increases, and this variation is highly correlated with PT incorporation content. Among all groups, the PG1 sample shows the weakest frost resistance, attaining a mass loss rate of 10.8% after 50 freeze–thaw cycles, where 62.1% of the total mass loss occurs within the initial 20 cycles. Such a phenomenon is fundamentally attributed to the intrinsic properties of phosphorus tailings. XRD results demonstrate that PT are mainly composed of crystalline minerals including dolomite, quartz and fluorapatite, which feature low cementitious reactivity, insufficient hydration products and loose matrix structure. During freeze–thaw cycling, volume expansion stress induced by the freezing of pore water easily damages interparticle bonding and triggers surface spalling, which serves as the primary cause of its severe early-stage mass loss [23]. Elevating the GGBS dosage can effectively enhance the freeze–thaw durability of binary composite binders. When the GGBS proportion reaches 40%, the sample only exhibits a mass loss rate of 6.3% after 50 freeze–thaw cycles. This value is 41.7% lower than that of the PG1 group, corresponding to the best freeze–thaw resistance

among all tested mixtures. Such performance improvement can be tentatively ascribed to the synergistic effect of high-activity GGBS. Abundant CaO, SiO_2 and Al_2O_3 contained in GGBS undergo hydration reactions under alkaline activation to generate substantial C-S-H gels. These gel phases fill internal pores, optimize pore structure and reduce the content of pore water. Meanwhile, the bonding effect of gels strengthens interparticle connection strength and effectively disperses structural damage induced by frost heaving stress. Nevertheless, when the dosage of GGBS exceeds 40%, the mass loss rate rebounds to 7.1%, which is 12.7% higher than that of PG5. This tendency can be explained by two reasons. Firstly, given the fixed dosage of alkaline activators, excessive GGBS may cause relatively limited alkalinity per unit of reactive solid. Consequently, part of the GGBS cannot be fully hydrated and merely acts as physical filler rather than participating in the construction of the gel network. Secondly, the mismatched particle gradation between GGBS and PT generates more internal microcracks, and crack propagation during freeze–thaw cycles aggravates mass loss [24].

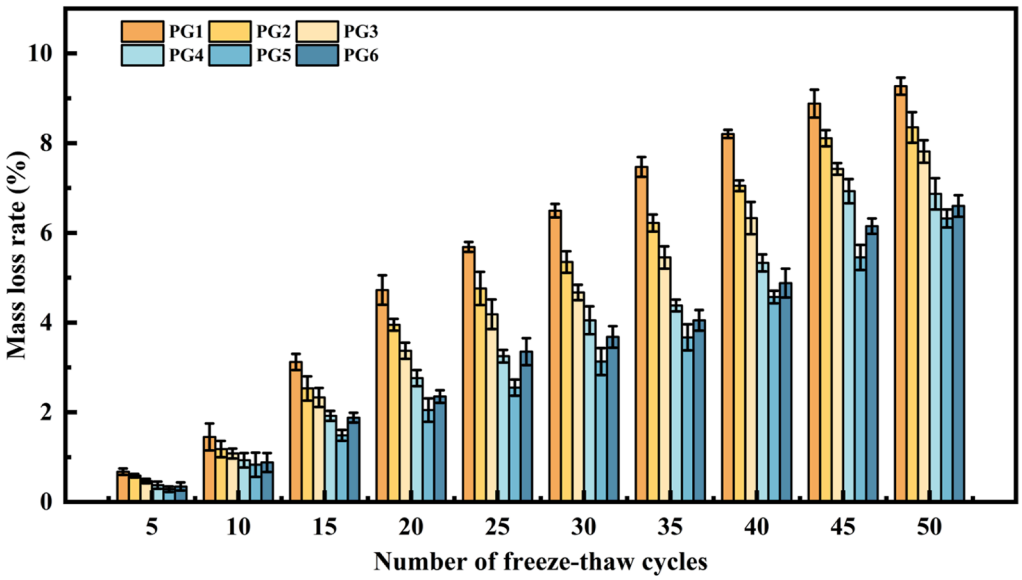


Figure 6. Mass loss rate of PT-GGBS binary cementitious materials during freeze–thaw cycles.

3.1.5. The Microscopic Characterization of PG

SEM-EDS was adopted to characterize the internal microstructures of three 28-d-cured binary cementitious specimens (Figure 7). In this section, tests were carried out only on representative specimens (PG1, PG5, PG6), covering conditions with low, medium and high levels of mineral powder content. These microscopic observation results are derived from representative specimens and cannot be generalized to all mix proportions in the binary test matrix. Mixing ratio imposes a significant effect on microstructural evolution. PG1 (Figure 7a) shows a loose microstructure filled with abundant unreacted PT particles. Low yield of cementitious products leads to weak inter-particle bonding and large pores, indicating that pure PT deliver a low alkali-activation degree and cannot form a dense matrix. Incorporation of GGBS greatly optimizes the microstructure, as substantial cementitious products fill intergranular voids and strengthen particle bonding. PG5 (Figure 7b) possesses plentiful, uniformly distributed gels and few residual unreacted particles, demonstrating the synergistic effect between GGBS and PT. Composite alkaline activators boost the hydration of both raw materials and stimulate sufficient gel formation. Combined SEM-EDS analysis confirms abundant interlaced gels in PG5, which fill internal pores and densify the matrix [25]. Accordingly, it is hypothesized that the incorporation of GGBS stimulates the geopolymerization reaction and generates considerable C-S-H

gels, which constitutes the tentative microscopic mechanism responsible for the strength enhancement of the binary system. In comparison with the single phosphorus-tailings system, both the efficiency of alkali-activated reactions and the quality of the formed microstructure are greatly improved in the composite system.

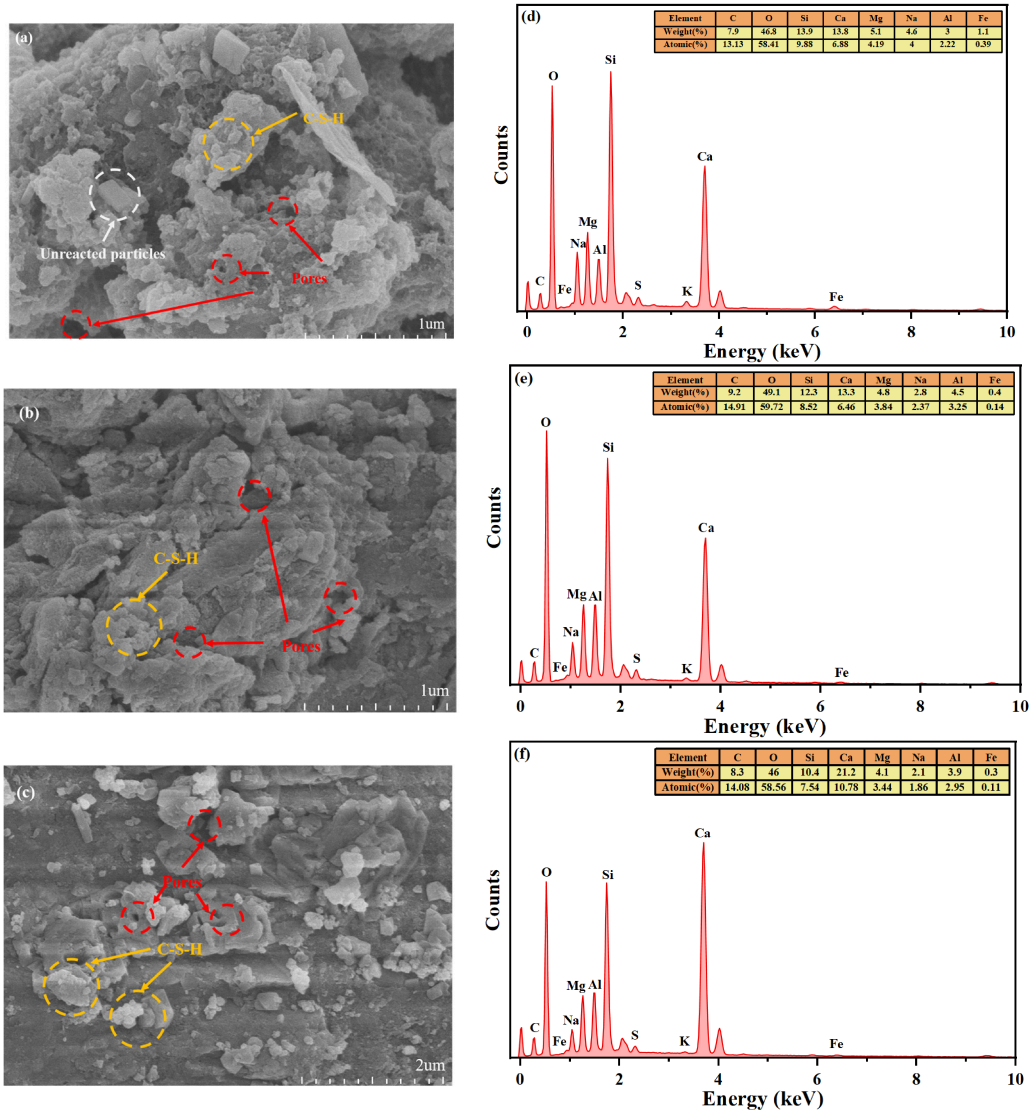


Figure 7. SEM images and EDS spectra of PT-based binary cementitious materials: PG1 (**a**,**d**), PG5 (**b**,**e**), PG6 (**c**,**f**).

3.1.6. The XRD and FTIR of PG

XRD tests were carried out on binary cementitious materials with various PT dosages cured for 28 days, and the test results are presented in Figure 8a. Overall, the positions of diffraction peaks for the three specimens are basically identical, demonstrating that they possess identical principal crystalline phases dominated by quartz (SiO_2), calcite ($CaCO_3$) and dolomite ($CaMg(CO_3)_2$), without obvious newly generated crystalline phases. It reveals that the primary reactions within the binary system consist of the generation of amorphous gels and structural rearrangement of inherent minerals, rather than the massive formation of new crystalline hydration products [26]. PG1 presents the sharpest quartz and dolomite peaks, reflecting abundant unreacted raw minerals and low alkali-activation degree. PG5 displays obviously reduced intensities of these mineral peaks, suggesting much more adequate reactions. Further increasing GGBS dosage raises the above-mentioned peak

intensities for PG6, demonstrating that excessive GGBS inhibits alkali-activated reactions. Consequently, although the three binary samples share identical main-phase assemblages, optimized mix proportions presumably facilitate continuous accumulation of C -S-H gels and gradual reduction in mineral diffraction intensity, eventually yielding a denser cohesive matrix structure.

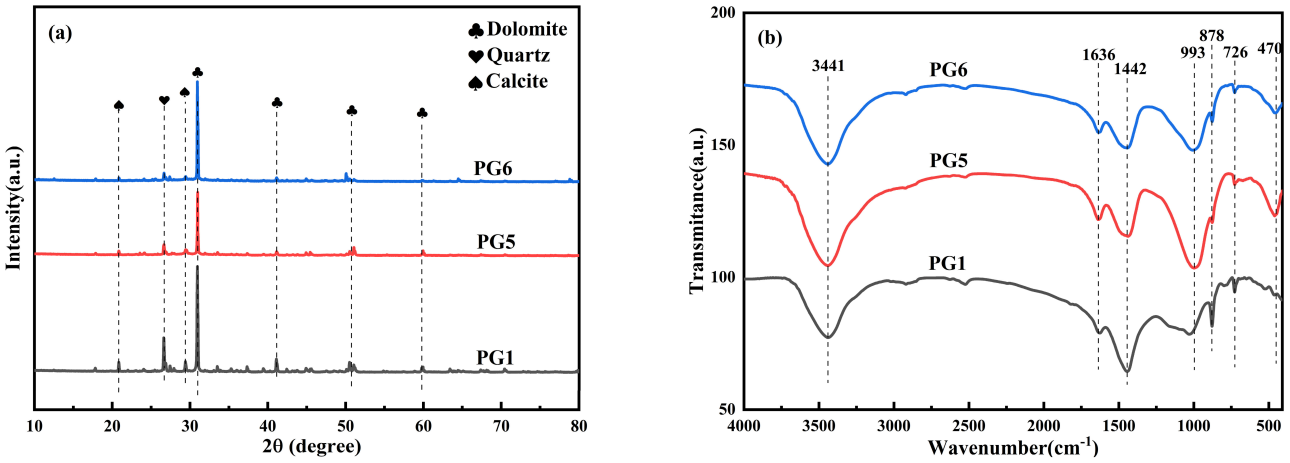


Figure 8. (**a**) XRD diagram and (**b**) FTIR diagram of PT-based binary cementitious materials with different compositions.

Figure 8b displays the FTIR spectra of PT-based binary cementitious materials cured for 28 d. The absorption bands centered at 3441 cm^{-1} and 1636 cm^{-1} are associated with bound water and adsorbed water, corresponding to the stretching vibration and bending vibration of O-H bonds, respectively [27]. The characteristic peak at 993 cm^{-1} originates from the asymmetric stretching vibration of Si-O-T bonds (T represents tetrahedral Si) within C-S-H gels, which serves as the signature peak of geopolymeric cementitious frameworks [28]. The absorption peaks at 1442 cm^{-1}, 878 cm^{-1} and 726 cm^{-1} are assigned to the vibrational modes of CO_3^{2-} groups in dolomite [3]. The band at 470 cm^{-1} corresponds to the bending vibration of Si-O/Al-O bonds [29]. Relative to pure-phosphorus-tailings PG1, GGBS addition intensifies and shifts characteristic peaks, confirming enhanced Al incorporation into silicate networks and the formation of C-S-H-dominated cementitious matrices. PG6 exhibits relatively high yet scattered Si-O-T peak intensity, indicating co-existing well-formed gels and incompletely reacted raw minerals and poor structural homogeneity. In contrast, PG5 yields concentrated main absorption bands, weakened primary-mineral peaks and distinct peak red-shift. It is tentatively inferred that PG5 forms a more homogeneous and continuous gel network and achieves a higher degree of hydration reaction.

3.2. Properties of Ternary Cementitious Materials Based on Phosphorus Tailings

As a typical pozzolanic material, fly ash can clearly optimize the pore structure and workability of cementitious systems through its morphological effect and physical filling effect. Accordingly, on the basis of PG5 (the best-performing mix within the tested binary compositional range), FA was incorporated into the PT-GGBS system to fabricate ternary composite cementitious materials. The influences of FA dosage on the workability, mechanical properties and durability of the prepared composites were systematically investigated, and the underlying hydration reaction mechanism was clarified combined with microscopic characterizations.

3.2.1. The Flowability and Compressive Strength of PGF

Figure 9a displays the fluidity changes of PT-based ternary cementitious composites. The test results demonstrate that increasing FA content leads to a steady decline in the fluidity of the ternary blending systems. The maximum fluidity of 176 mm is achieved at a FA dosage of 4%, whereas the fluidity declines to 160 mm when the FA content rises to 24%, corresponding to an overall reduction of 9.1%. In practical engineering applications, extra water is usually supplemented together with FA incorporation; however, no additional water was supplied in the present experiment. It is hypothesized that FA consumes a large quantity of free water during its reaction, which reduces the available free water, raises the overall viscosity of fresh paste and consequently reduces fluidity. Nevertheless, despite the downward trend in fluidity, the ternary systems still maintain a relatively high fluidity level compared with sample PG5. Although FA incorporation theoretically reduces the water demand of the system, partial replacement of GGBS alleviates the strong water adsorption induced by the high specific surface area of GGBS, thereby preserving the flowability of fresh paste to a certain extent. In summary, the fluidity of the ternary system decreases continuously as FA dosage increases.

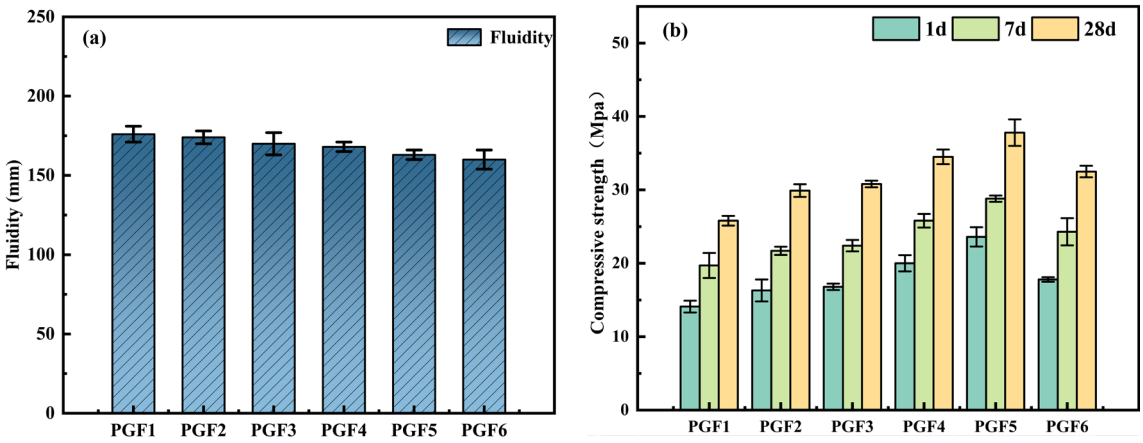


Figure 9. (**a**) Flowability and (**b**) compressive strength of PT-mineralpowder-FA ternary cementitious materials.

As presented in Figure 9b, the compressive strength of ternary cementitious materials first increases remarkably, then declines obviously with the rising FA dosage. The optimal compressive strength is obtained at a FA dosage of 20% (PGF5), with values of 23.6 MPa, 28.8 MPa and 37.8 MPa at 1 day, 7 days and 28 days, respectively. These strengths are increased by 67.4%, 46.2% and 46.5% relative to PGF1, showing a prominent strengthening effect. This result verifies that FA works synergistically with PT and GGBS under alkaline activation. It is tentatively proposed that abundant reactive SiO_2 and Al_2O_3 in FA undergo pozzolanic reactions under the alkaline environment supplied by CaO released from GGBS, generating abundant C-S-H and C-A-S-H gels and greatly improving mechanical strength. Nevertheless, further increasing FA dosage to the PGF6 group leads to an obvious drop in compressive strength. The compressive strengths of PGF6 at all curing ages are lower than those of the optimal PGF5 group: 17.8 MPa at 1 d, 24.3 MPa at 7 days and 32.5 MPa at 28 days, which are decreased by 24.6%, 15.6% and 14.0% in comparison with PGF5. This evolution indicates an optimal dosage threshold for strength improvement in this PT-based ternary system. Excessive FA replaces a portion of highly reactive GGBS and PT, reducing the total content of reactive components per unit volume and resulting in strength degradation [30]. In conclusion, appropriate incorporation of FA can effectively enhance the compressive strength of PT-GGBS composite cementitious materials. For PGF1 and PGF5 in the ternary

system, the standard deviation and coefficient of variation for the compressive strength values at 28 days were (SD = 0.66 MPa, CV = 2.56%) and (SD = 1.80 MPa, CV = 4.76%), respectively. These variations fall within the acceptable range for geopolymer testing.

To assess actual competitiveness, this paper uses ordinary Portland cement mortar (P·O 42.5) blended with 30 per cent PT as a preliminary benchmark [31]. The aim is to provide a simple comparison of the performance of two cementitious systems containing the same solid waste but differing in composition. The maximum 28-day compressive strength of this mortar is 41.1 MPa. The compressive strength of our optimized ternary geopolymer was 37.8 MPa, representing 92% of that of the PT cement mortar. This is considered acceptable for a material composed entirely of solid waste.

3.2.2. The Drying Shrinkage and Mass Loss of PGF

As illustrated in Figure 10a, specimen PGF1 exhibits the most severe drying shrinkage. Its shrinkage rate reaches 0.56% at 5 days and rises to 1.17% at 30 d, which is the maximum value among all ternary cementitious mixtures. In contrast, PGF5 achieves the optimal volume stability with a 30 days drying shrinkage rate of merely 0.76%, a reduction of 0.41% relative to PGF1. This indicates that material microstructure influences the volume-stability behavior of the binder. When the FA dosage exceeds 20% (PGF6), its 30 day drying shrinkage rate increases by 26.21% compared with PGF5. This phenomenon can be tentatively explained as follows: At a fixed activator dosage, excessive FA presumably gives rise to relative alkali limitation against the increased reactive solid content, such that a fraction of FA only serves as physical filler instead of participating in hydration reactions. More internal micropores are presumably formed, providing additional channels for water evaporation during the drying process and consequently raising the drying-shrinkage rate.

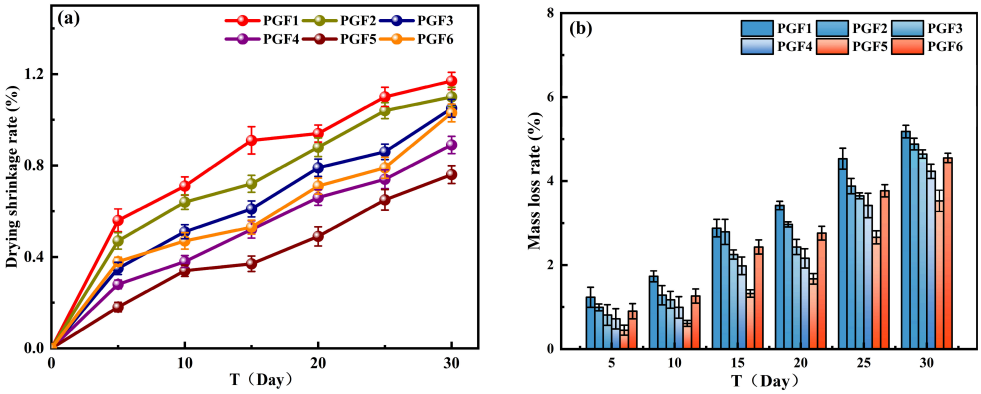


Figure 10. Drying shrinkage and mass loss properties of PT-GGBS-FA ternary cementitious composites: (**a**) Drying shrinkage characteristics of ternary binders; (**b**) Mass loss characteristics of ternary binders.

Figure 10b reveals that FA dosage imposes a notable influence on the mass loss rate of the ternary composites. PGF1 maintains a relatively high mass loss rate throughout the curing period, reaching 5.18% at 30 d; PGF5 possesses the minimum mass loss rate of 3.53% at 30 d, which is 31.9% lower than that of PGF1. When the FA dosage is further increased to 24%, the 30-day mass loss rate of PGF6 rebounds to 4.55%. It can be concluded that introducing a reasonable amount of FA can further optimize the structural compactness and volume stability of the binary cementitious system.

3.2.3. The Mass Loss During the Wet–Dry Cycle of PGF

Figure 11 presents the evolution of mass loss rate of PT-GGBS-FA ternary cementitious materials subjected to 30 drying–wetting cycles. From the overall evolutionary trend, the mass-loss ratio for every sample group keeps climbing as the freeze–thaw cycle count goes

up. For the initial 0–10 cycles, all test specimens show mass loss below 2.0% and exhibit a relatively slow rising trend. The phase spanning 10–25 cycles is identified as the rapid degradation stage, in which cumulative mass loss surges remarkably. Afterwards, the increment becomes obviously suppressed over 25–30 cycles, and the mass-loss value tends toward a steady state.

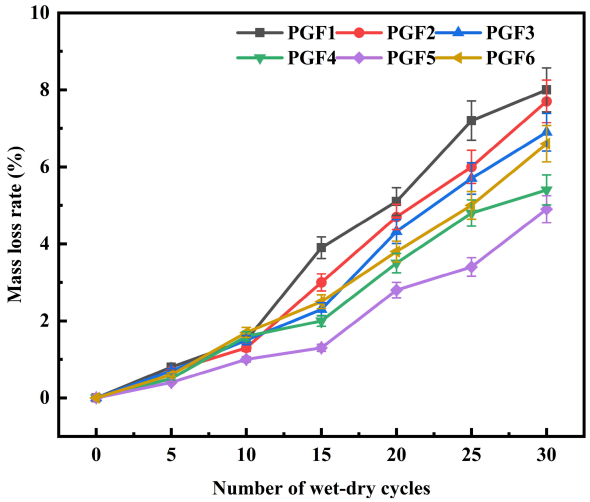


Figure 11. Mass loss rate of PT-GGBS-FA ternary cementitious materials during dry and wet cycles.

Regarding the effect exerted by FA incorporation, the drying–wetting durability presents an upward-then-downward trend as the fly ash proportion keeps increasing. When the FA dosage increases gradually from 4% to 20%, the cumulative mass loss rates after 30 cycles are 8.0%, 7.7%, 6.9%, 5.4% and 4.9%, respectively, showing a continuous declining trend. Specimen PGF5 with 20% FA exhibits the optimal resistance against drying–wetting cycles, with a mass loss rate of only 4.9% after 30 cycles, which is 38.8% lower than PGF1 with the minimum FA addition. Moreover, PGF5 achieves the lowest mass loss rate at all cyclic stages, with values of merely 1.3%, 2.8% and 3.4% after 15, 20 and 25 cycles, respectively, far lower than other groups at identical cycles, with lower mass-loss values under cyclic drying–wetting exposure relative to other tested PGF. The essential mechanism lies in that appropriate FA optimizes the pore structure and enhances matrix compactness relying on its pozzolanic reactivity and micro-aggregate filling effect, which effectively retards the initiation and propagation of microcracks during cyclic exposure and thereby greatly strengthens the durability against drying–wetting cycles [32]. Nevertheless, further incorporation of FA beyond 20% degrades the cyclic resistance, and the cumulative mass loss rebounds to 6.6% after 30 cycles, representing a 34.7% increment relative to the optimal PGF5 group. Its mass loss rate remains higher than PGF4 and PGF5 once the cycle number exceeds 10. This phenomenon indicates that excessive supplementary cementitious materials lead to insufficient hydration reactions of the whole system; excessive FA weakens the early hydration activity, and unhydrated particles act as internal structural defects, accelerating crack initiation and propagation under cyclic stress and ultimately deteriorating the durability performance [33]. In conclusion, rational incorporation of FA effectively enhances the drying–wetting resistance of PT-based ternary cementitious composites.

3.2.4. The Resistance to Freeze–Thaw Cycles of PGF

Figure 12 shows the mass-loss evolution of PT-GGBS-FA ternary binder composites subjected to 50 freeze–thaw cyclic treatments. Compared with the binary PT–GGBS system, the freeze–thaw resistance of the ternary system is greatly improved overall, and the regulation effect of FA dosage on frost resistance exhibits obvious nonlinear characteristics. The

optimal freeze–thaw performance is achieved at a FA dosage of 20%. After 50 freeze–thaw cycles, its cumulative mass loss rate is merely 3.8%, which is 40.0% lower than PG5 (the optimal specimen in the binary system) and 49.3% lower than PGF1 with the lowest FA content in the ternary system, showing a remarkable enhancement in frost resistance. The intrinsic mechanisms responsible for performance improvement are elaborated from two perspectives. On the one hand, substantial reactive SiO_2 and Al_2O_3 originating from FA participate in secondary alkali-activated reactions. Driven by CaO liberated from GGBS within the alkaline circumstance, denser C-S-H gels are produced. Such reaction products further fill the incompletely closed capillary pores inside the binary matrix and cut down the storage capacity for pore water [34]. On the other hand, a large number of spherical FA particles are uniformly dispersed within the matrix. These spherical particles alleviate local stress concentration induced during freeze–thaw cycling via the "stress buffering effect" and restrain the initiation and propagation of microcracks [35]. When the FA dosage is less than 12%, the improvement in freeze–thaw resistance of the ternary system is quite limited. Taking specimen PGF1 as an example, its cumulative mass loss rate reaches 7.5% after 50 cycles, only 12.7% lower than the optimal binary sample PG5, indicating insignificant optimization of frost resistance. Insufficient FA provides inadequate reactive components, which fail to exert effective filling and cementing effects; accordingly, the pore structure cannot be optimized substantially. Frost heaving stress still causes severe structural deterioration, resulting in a relatively high mass loss rate. Excessive FA addition above 20% leads to distinct degradation of freeze–thaw resistance and a rebound in mass loss rate. After 50 freeze–thaw cycles, the PGF6 group yields a mass loss rate of 5.2%, which is 36.8% higher than that of the optimal PGF5 group. Excessive FA incorporation significantly increases the water requirement of the composite mixture and markedly raises the proportion of closed pores within the matrix. During freeze–thaw cycling, the volume expansion of frozen water confined in closed pores fails to release accumulated stress via seepage, thereby exacerbating local structural damage, elevating mass loss, and ultimately deteriorating the frost resistance of the geopolymer material [36].

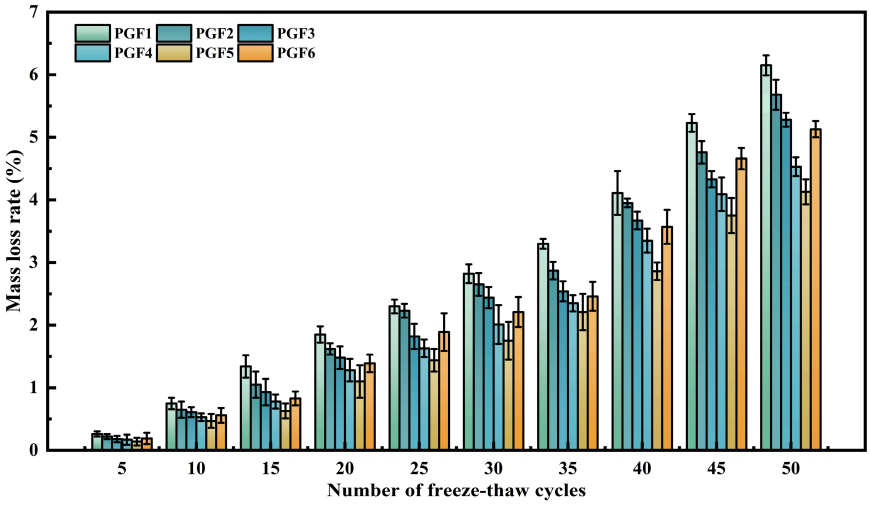


Figure 12. Mass loss rate of PT-GGBS-FA ternary cementitious materials during freeze–thaw cycle.

3.2.5. The Microscopic Characterization of PGF

SEM-EDS was employed to characterize the internal microstructures of 28-day cured PT-GGBS-FA ternary specimens, as shown in Figure 13. In this section, tests were conducted using only three representative specimens (PGF1, PGF5 and PGF6), representing low, medium and high fly ash content levels. The results of the microscopic observations are based on a selection of representative specimens and cannot be extrapolated to all test

mix proportions in the trinary system. Noticeable micromorphological differences among samples directly correlate with their macroscopic mechanical and durability performances. PGF1 (Figure 13a) possesses a highly defective microstructure. Numerous angular unreacted PT and GGBS particles suggest inadequate alkali-activated reactions. Scattered flocculent C-S-H gels merely attach to partial particle surfaces without forming a continuous bonding network, and abundant large, interconnected pores and microcracks result in poor matrix compactness. PGF6 (Figure 13c) shows microstructural improvement relative to PGF1 yet retains prominent defects. Despite partial C-S-H gel formation, abundant unhydrated spherical fly ash particles persist in the matrix. Unevenly distributed gels only function as local binders and cannot fully fill inter-particle voids, accompanied by visible cracks. With unchanged activator dosage, excessive FA may result in limited available alkalis relative to reactive phases, so that the pozzolanic activity of partial FA cannot be fully triggered. Remaining unhydrated particles serve as internal defects, facilitating crack propagation under drying–wetting or freeze–thaw cyclic loading and degrading macroscopic durability [37]. By comparison, PGF5 (Figure 13b) delivers the optimal microstructure, where sufficient C-S-H gels construct a dense continuous network. Interwoven gels adequately fill inter-particle voids and embed residual mineral particles into a monolithic matrix. The proportion of residual unreacted particles is greatly reduced; the pore structure is markedly refined with smaller pore sizes and drastically decreased pore quantity, forming a continuous, dense microstructure free of obvious structural flaws.

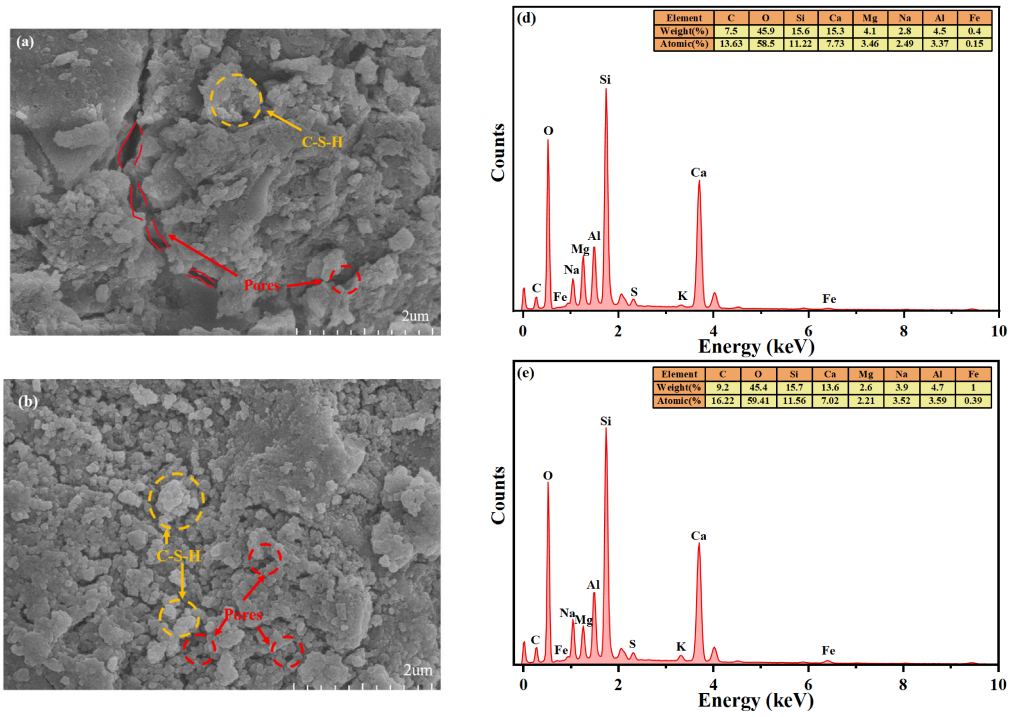


Figure 13. *Cont.*

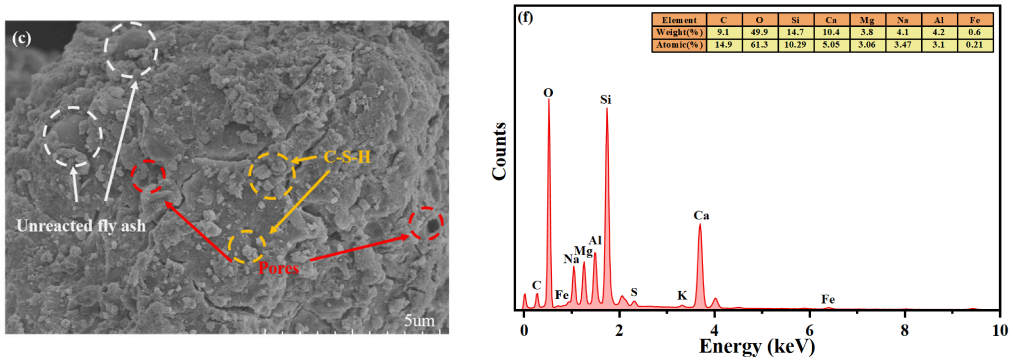


Figure 13. SEM images and EDS spectra of PT-based ternary cementitious materials: PGF1 (**a**,**d**), PGF5 (**b**,**e**), PGF6 (**c**,**f**).

It can be tentatively concluded that the ternary system with this mixing ratio achieves a high degree of alkali-activated reaction. The pozzolanic reactivity and micro-aggregate-filling effect of FA are presumably fully exploited, and the strong-bonding effect of cementitious products effectively improves the mechanical performance and durability of the composite material.

3.2.6. The XRD and FTIR of PGF

XRD was conducted on 28-day cured ternary cementitious materials with varied FA contents (Figure 14a). PGF1, PGF5 and PGF6 show nearly consistent diffraction peak positions, with quartz, calcite and dolomite as the main crystalline phases. Sharp, strong peaks of quartz and carbonates in PGF1 indicate inadequate involvement of reactive components in alkali-activation. At the PGF5 fly ash dosage, obvious reduction in mineral diffraction intensity and mild peak broadening confirm that appropriate fly ash addition promotes alkali-activated reactions and yields large amounts of cementitious gels. PGF6 exhibits marginally lower mineral peak intensities than PGF1, and amorphous gels still dominate the matrix. Further fly ash elevation renders calcium the reaction-limiting factor and stabilizes gel-formation rate. Residual primary minerals such as dolomite do not display monotonic intensity changes with fly ash dosage. Comprehensive analysis tentatively confirms that increasing fly ash dosage facilitates the formation of gel products in the ternary composites, whereas excessive FA imposes restrictions on gel generation, and PGF5 achieves the highest degree of alkali-activated cementitious reaction among the three groups.

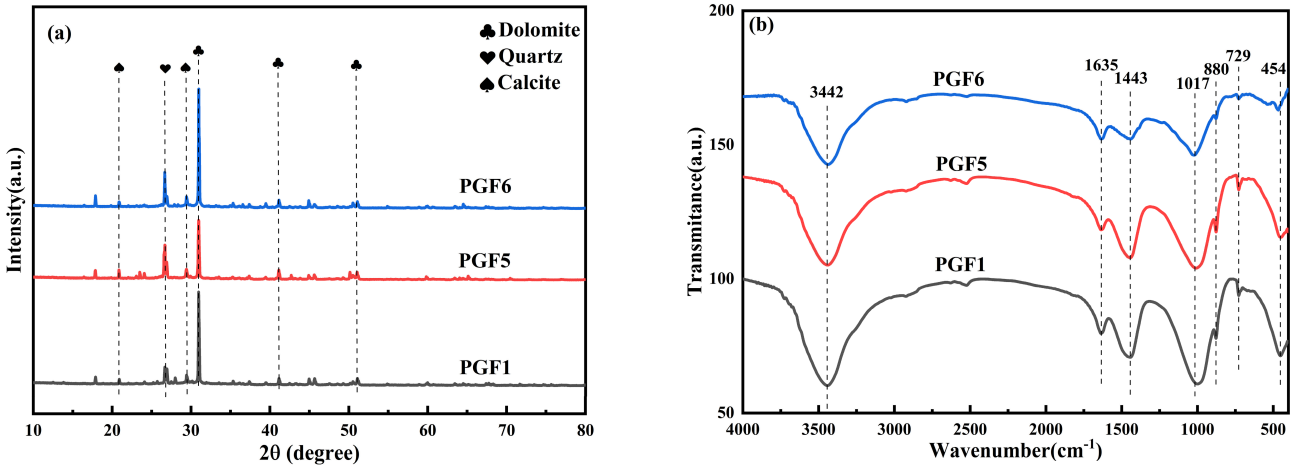


Figure 14. (**a**) XRD diagram and (**b**) FTIR diagram of PT-based ternary cementitious material with different compositions.

FTIR tests were conducted on PGF1, PGF5 and PGF6 cured for 28 days to clarify the reaction characteristics and structural evolution of PT-GGBS-FA ternary cementitious systems under alkali activation. As shown in Figure 14b, a broad absorption band centered at approximately 3442 cm^{-1} is observed for all specimens, corresponding to the stretching vibration of interlayer water within C-S-H gels, while the bending vibration of bound water appears at 1635 cm^{-1} [38]. The bands at 1017 cm^{-1} and 880 cm^{-1} are assigned to the asymmetric stretching vibration of Si–O–T bonds (T denotes tetrahedrally coordinated Si or Al) in C(N)-A-S-H gels [39]. Compared with the Si-O-Si vibration peaks of raw minerals, this characteristic band shifts toward lower wavenumbers, the observed band shift is indicative of aluminum potentially being incorporated into the silicate tetrahedral network, and is consistent with the development of an aluminosilicate-type gel-like framework. It should be noted that FTIR alone cannot provide definitive phase discrimination between closely-related amorphous geopolymer gel phases. The absorption peaks near 1443 cm^{-1} and 729 cm^{-1} originate from the vibrational modes of carbonate CO_3^{2-} groups [4]. Comparative analysis indicates that PGF5 exhibits superior stability in the peak position and concentrated peak profile of the principal Si-O-T band, together with a continuous vibration band near 454 cm^{-1}, which evidences a more homogeneous and integrated aluminosilicate gel network. By contrast, although the other two specimens also display obvious signatures of cementitious reactions, they fail to achieve optimal reaction sufficiency and structural uniformity, which can be attributed to the existence of partially unreacted primary mineral phases. Overall interpretation of FTIR spectral features tentatively verifies that the PGF5 ternary composite possesses the most favorable reaction degree and structural configuration at the microscopic scale.

In summary, according to the compressive strength and durability test results, the optimized ternary geopolymer (PGF5, 28-d compressive strength of 37.8 MPa) exhibits low drying shrinkage and excellent resistance to wet–dry and freeze–thaw cycles. It shows potential research prospects for developing precast municipal components such as sidewalk paving bricks, curb stones, drainage components, slope-protection blocks, non-load-bearing building blocks and high-grade masonry mortar for open-air service conditions with wet–dry alternation and seasonal freeze–thaw. Further validation including leaching test, comprehensive durability evaluation and pilot-scale trial is required before practical engineering application.

Overall, the performance evolution of binary and ternary alkali-activated geopolymers is synergistically governed by gel formation, pore structure refinement, particle packing optimization and alkali reaction degree. Appropriate mineral powder and fly ash incorporation promote the formation of dense C-S-H gel products, which fill internal pores, reduce structural defects, and densify the matrix microstructure. Optimized particle gradation further improves the compactness of the powder system. In contrast, excessive solid waste dosage relatively reduces effective alkalinity, limits geopolymer reaction degree and induces increased pores and microcracks, thereby deteriorating macroscopic mechanical and durability performance. These comprehensive microstructural changes dominate the variation trends of strength, drying shrinkage and cyclic durability.

4. Conclusions

In this work, binary PT-GGBS and ternary PT-GGBS-FA alkali-activated geopolymers were prepared. The effects of solid-waste blending on workability, mechanical performance and durability were investigated, and the synergistic geopolymerization mechanism was revealed via multi-scale microscopic characterizations. Within the investigated binary compositional window, the binary system achieved the best comprehensive performance at 40% GGBS replacement. Further incorporating 20% FA into this binary reference improved

both mechanical strength and durability of the resulting ternary geopolymer. GGBS supplies reactive calcium to trigger the formation of C-S-H gels. FA provides additional reactive silicon–aluminum species for secondary pozzolanic reactions, and refines pore structures through complementary particle gradation and micro-aggregate filling. Matrix densification originates from the coupling of chemical gel formation and physical packing effects. The optimized ternary geopolymer achieves high compressive strength together with mitigated drying shrinkage and improved resistance to wet–dry and freeze–thaw cycles, exhibiting potential prospects for the future development of precast municipal components and non-load-bearing building blocks, pending further safety and durability validation.

5. Limitation and Suggestion for Future Studies

Despite promising laboratory-scale performance, several critical barriers remain before large-scale practical engineering implementation. Environmental safety risk: PT contain phosphorus, fluorine and trace heavy-metal elements. This study did not perform systematic leaching-toxicity tests. The long-term element-release risk under rainwater and groundwater erosion remains unclear, which is an essential prerequisite for the engineering utilization of tailings-based building materials. Missing carbon-emission and cost evaluation: Life-cycle carbon footprint and economic-cost assessment for the whole manufacturing chain are not included in the present work. Alkali activators (sodium silicate, sodium hydroxide) have relatively high embodied energy and cost, which may offset the low-carbon merits of geopolymers. Further activator optimization and full-chain LCA analysis are required. Engineering-scale and manufacturing constraints: All tests were conducted on small-scale laboratory specimens. Verification under real-service conditions, large-size component performance and in situ casting adaptability are lacking. This material is more suitable for factory precasting, while its feasibility for on-site casting still needs further investigation. Regarding durability evaluation of wet–dry and freeze–thaw cycles, only specimen mass-loss rate was measured in this study, which mainly reflects surface spalling damage. Important supplementary durability indicators including residual compressive strength, relative dynamic modulus of elasticity, ultrasonic pulse velocity and systematic visual-damage grading were not tested. Consequently, the present test results cannot serve as a comprehensive assessment of long-term durability. Future work should incorporate these multi-index durability characterizations to achieve more complete deterioration evaluation. Due to the limited number of test formulations, this study was unable to establish a statistically significant quantitative relationship between workability, compressive strength and durability. Consequently, a multi-criteria qualitative comparison method was employed to identify the mix with the best performance within the test range. To establish a reliable predictive relationship, it will be necessary to expand the database and include additional mix design points; this remains a key focus for future research. A further limitation of the experiment lies in the selection of the reference mixture. In this study, the 100% phosphate tailings sample (PG1) was used solely as an internal reference for relative comparisons between the binary mixtures under test. It did not serve as a standardized external control. The inclusion of dedicated external reference groups (such as ordinary Portland cement-based binders and non-activated precursor mixtures) was not incorporated into this experimental design, which limited the ability to strictly distinguish between the contribution of alkali activation and the inherent material effects derived from the phosphate tailings precursor. Future work will incorporate such standard reference groups to enable more reliable performance benchmarking. Furthermore, SEM-EDS micro-characterization was carried out only on a small number of representative samples, and the qualitative assessment of the pore structure based on scanning electron microscope images reflects only superficial characteristics. Future research will involve quantitative characterization of

pore structure, such as the mercury intrusion porosimetry (MIP) method or pore analysis based on scanning electron microscope images, in order to obtain reliable quantitative data on pore size distribution.

Future work will focus on pore analysis, long-term leaching stability testing of hazardous elements, life-cycle carbon emissions and cost analysis, the development of low-cost and energy-efficient activators and pilot-scale component experiments, with a view to advancing the transition of PT-based geopolymer technology from laboratory research to practical engineering applications.

Author Contributions: Conceptualization, H.L.; Methodology, B.-J.H.; Software, Z.W.; Formal analysis, J.W.; Resources and Data curation, Q.D.; Data curation and Writing—original draft, Y.Z. All authors have read and agreed to the published version of the manuscript.

Funding: This study was supported by the Postgraduate Research & Practice Innovation Program of Jiangsu Province, grant numbers (SJCX25_2103).

Data Availability Statement: The original contributions presented in this study are included in the article. Further inquiries can be directed to the corresponding authors.

Conflicts of Interest: The authors declare no conflicts of interest.

References

1. Odeh, A.; Al-Fakih, A.; Alghannam, M.; Al-Ainya, M.; Khalid, H.; Al-Shugaa, M.A.; Thomas, B.S.; Aswin, M. Recent progress in geopolymer concrete technology: A review. *Iran. J. Sci. Technol. Trans. Civ. Eng.* **2024**, *48*, 3285–3308. [CrossRef]
2. Yu, Y.-H.; Du, C.-M.; Zhang, Y.-T.; Yuan, R.-Y. Phosphorus recovery from phosphorus tailings through a two-stage leaching-precipitation process: Toward the harmless and reduction treatment of P-bearing wastes. *Environ. Res.* **2024**, *248*, 118328. [CrossRef] [PubMed]
3. Moukannaa, S.; Loutou, M.; Benzaazoua, M.; Vitola, L.; Alami, J.; Hakkou, R. Recycling of phosphorus mine tailings for the production of geopolymers. *J. Clean. Prod.* **2018**, *185*, 891–903. [CrossRef]
4. Zhang, S.-X.; Xie, X.; Xie, R.-Q.; Tong, X.; Wu, Y.-Y.; Li, J.-W.; Li, Y. Preparation and interface state of phosphorus tailing-based geopolymers. *J. Cent. S. Univ.* **2024**, *31*, 1900–1914. [CrossRef]
5. Shi, Y.; Jiang, F.; Wang, R.; Yang, S.; Zhu, X.; Shen, Y. A mini review on the separation of Al, Fe and Ti elements from coal fly ash leachate. *Int. J. Coal Sci. Technol.* **2024**, *11*, 24. [CrossRef]
6. Obeng, J.; Andrews, A.; Adom-Asamoah, M.; Adjei, S. Effect of calcium carbide residue on the sulphate resistance of metakaolin-based geopolymer mortars. *Clean. Mater.* **2023**, *7*, 100177. [CrossRef]
7. Zheng, K.; Zhou, J.; Gbozee, M. Influences of phosphorus tailings on hydration and properties of Portland cement. *Constr. Build. Mater.* **2015**, *98*, 593–601. [CrossRef]
8. Yimiao, N.; Miao, X.; Panpan, L.; Ling, W.; Shuxian, L.; Sen, W.; Yingchun, W.; Shuoyu, L.; Peixin, Z. Research progress on fly ash based geopolymer. *Multipurp. Util. Miner. Resour.* **2022**, *43*, 123–128.
9. Chen, X.; Zhang, J.; Lu, M.; Chen, B.; Gao, S.; Bai, J.; Zhang, H.; Yang, Y. Study on the effect of calcium and sulfur content on the properties of fly ash based geopolymer. *Constr. Build. Mater.* **2022**, *314*, 125650. [CrossRef]
10. Khouadjia, M.L.K.; Mezghiche, B.; Drissi, M. Experimental evaluation of workability and compressive strength of concrete with several local sand and mineral additions. *Constr. Build. Mater.* **2015**, *98*, 194–203. [CrossRef]
11. Song, Y.; Zhang, J.; Wu, H.; Yang, C.; Jia, D.; Wei, W. All-solid-waste alkali-activated materials: A critical review of multi-waste synergy, heavy metal stabilization, and sustainable engineering applications. *J. Environ. Chem. Eng.* **2025**, *13*, 119204. [CrossRef]
12. Wang, Z.; He, Y.; Luo, H.; Wang, Q.; Sun, H.; Song, H.; Zhao, X.; He, B.-J. Phosphorus Tailings Sand Synergized with Multiple Solid Wastes for the Preparation of Cementitious Materials: Properties and Mechanisms. *Buildings* **2026**, *16*, 521. [CrossRef]
13. *GB/T 17671-2021*; Test Method of Cement Mortar Strength (ISO Method). Standards Press of China: Beijing, China, 2021.
14. *GB/T 8077-2023*; Methods for Testing Uniformity of Concrete Admixtures. Standards Press of China: Beijing, China, 2023.
15. *JGJ/T 70-2009*; Standard for Test Methods for Basic Properties of Construction Mortar. China Architecture & Building Press: Beijing, China, 2009.
16. *GB/T 50082-2009*; Standard Test Methods for Durability and Long-Term Performance of Ordinary Concrete. China Architecture & Building Press: Beijing, China, 2009.
17. Zhang, C.; Jiawei, W.; Zhang, X.; Hou, J.; Huang, J.; Shuxia, F.; Wang, J.; Duan, G. Influence of Limestone Powder on Water Film Thickness and Plastic Viscosity of Uhpc. *Case Stud. Constr. Mater.* **2024**, *20*, e03036. [CrossRef]

18. Shi, C.; Liu, Y.; Qin, L.; Ghafoor, M.T.; Zhang, Z. Time-dependent evolution of the microstructural characteristics of CASH and NASH gels with various Ca/Si and Al/Si ratios. *Constr. Build. Mater.* **2025**, *502*, 144408. [CrossRef]
19. Liu, B.; Meng, H.; Pan, G.; Zhou, H.; Li, D. Relationship between the fineness and specific surface area of iron tailing powder and its effect on compressive strength and drying shrinkage of cement composites. *Constr. Build. Mater.* **2022**, *357*, 129421. [CrossRef]
20. Gayathiri, K.; Praveenkumar, S. Retaining the particle packing approach and its application in developing the cement composites towards sustainability. *J. Build. Pathol. Rehabil.* **2023**, *8*, 26. [CrossRef]
21. Sun, Y.; Li, G.; Shu, J.; Qin, Y.; Tao, W. Experimental investigation on solid waste-based high performance soilcrete. *Constr. Build. Mater.* **2024**, *419*, 135501. [CrossRef]
22. Moula, S.; Fraj, A.B.; Wattez, T.; Bouasker, M.; Ali, N.B.H. Mechanical properties, carbon footprint and cost of ultra-high performance concrete containing ground granulated blast furnace slag. *J. Build. Eng.* **2023**, *79*, 107796. [CrossRef]
23. Shen, J.; Wang, Q.; Chen, Y.; Han, Y.; Zhang, X.; Liu, Y. Evolution process of the microstructure of saline soil with different compaction degrees during freeze-thaw cycles. *Eng. Geol.* **2022**, *304*, 106699. [CrossRef]
24. Wu, J.; Li, J.; Rao, F.; Yin, W. Mechanical property and structural evolution of alkali-activated slag-phosphorus mine tailings mortars. *Chemosphere* **2020**, *251*, 126367. [CrossRef] [PubMed]
25. Qi, F.; Zhu, G.; Zhang, Y.; Hou, X.; Li, S.; Zhang, J.; Li, H. Effect of calcium to silica ratio on the synthesis of calcium silicate hydrate in high alkaline desilication solution. *J. Am. Ceram. Soc.* **2021**, *104*, 535–547. [CrossRef]
26. Bernal, S.A.; Provis, J.L.; Brice, D.G.; Kilcullen, A.; Duxson, P.; Van Deventer, J.S. Accelerated carbonation testing of alkali-activated binders significantly underestimates service life: The role of pore solution chemistry. *Cem. Concr. Res.* **2012**, *42*, 1317–1326. [CrossRef]
27. Pradhan, P.; Dwibedy, S.; Pradhan, M.; Panda, S.; Panigrahi, S.K. Durability characteristics of geopolymer concrete-Progress and perspectives. *J. Build. Eng.* **2022**, *59*, 105100. [CrossRef]
28. Wang, Y.; Liu, X.; Zhang, W.; Li, Z.; Zhang, Y.; Li, Y.; Ren, Y. Effects of Si/Al ratio on the efflorescence and properties of fly ash based geopolymer. *J. Clean. Prod.* **2020**, *244*, 118852. [CrossRef]
29. Li, Z.; Ikeda, K. Compositions and microstructures of carbonated geopolymers with different precursors. *Materials* **2024**, *17*, 1491. [CrossRef] [PubMed]
30. Vairagade, V.S. Multi-scale theoretical modeling with molecular simulation framework for fly ash-based high-performance concrete. *Sci. Rep.* **2025**, *15*, 44895. [CrossRef] [PubMed]
31. Jiang, L.; Li, J.; Zhang, Q.; Yang, L.; Cao, J. Influence of phosphorus tailings fineness on the hydration process and physical properties of ordinary Portland cement. *Constr. Build. Mater.* **2024**, *417*, 135349. [CrossRef]
32. Luo, X.; Gao, J.; Guo, Z.; Li, S.; Liu, C.; Zhao, Y. Experimental study on the rheological property of cement paste with fly ash and brick powder. *Powder Technol.* **2023**, *426*, 118635. [CrossRef]
33. Zhang, S.; Duque-Redondo, E.; Kostiuchenko, A.; Dolado, J.S.; Ye, G. Molecular dynamics and experimental study on the adhesion mechanism of polyvinyl alcohol (PVA) fiber in alkali-activated slag/fly ash. *Cem. Concr. Res.* **2021**, *145*, 106452. [CrossRef]
34. Zeng, G.; Shu, B.; Qiu, B.; Qiu, K.; Luo, D. Dry-wet cycles durability of solid waste based cementing materials solidifying different characteristic soils. *Mater. Res. Express* **2024**, *11*, 055513. [CrossRef]
35. Xiao, Y.; Ju, X.; Li, C.; Wang, T.; Wu, R. Research on recycling of phosphorus tailings powder in open-graded friction course asphalt concrete. *Materials* **2023**, *16*, 2000. [CrossRef] [PubMed]
36. Liu, M.; Liu, H.; Zhu, P.; Chen, C.; Wang, X.; Xu, L. Recycling potential evaluation of geopolymer concrete with different cementitious system used in freeze-thaw environment. *Case Stud. Constr. Mater.* **2024**, *21*, e03535. [CrossRef]
37. Liu, B.; Li, J.; Dong, X.; Jia, X.; Xu, G.; Chen, J. Synergistic effects and mechanism analysis of ternary full-solid-waste geopolymer mortar. *Constr. Build. Mater.* **2026**, *532*, 146707. [CrossRef]
38. Bernal, S.A.; Provis, J.L.; Rose, V.; De Gutierrez, R.M. Evolution of binder structure in sodium silicate-activated slag-metakaolin blends. *Cem. Concr. Compos.* **2011**, *33*, 46–54. [CrossRef]
39. Shee-Ween, O.; Cheng-Yong, H.; Yun-Ming, L.; Abdullah, M.M.A.B.; Li-Ngee, H.; Pakawanit, P.; Khalid, M.S.; Muhammad, W.H.B.W.; Wan-En, O.; Yong-Jie, H. Green development of fly ash geopolymer via casting and pressing Approaches: Strength, Morphology, efflorescence and Ecological Properties. *Constr. Build. Mater.* **2023**, *398*, 132446. [CrossRef]

Disclaimer/Publisher's Note: The statements, opinions and data contained in all publications are solely those of the individual author(s) and contributor(s) and not of MDPI and/or the editor(s). MDPI and/or the editor(s) disclaim responsibility for any injury to people or property resulting from any ideas, methods, instructions or products referred to in the content.